Climate change attribution of the 2021 Henan extreme precipitation: Impacts of convective organization

Han QIN[1], Wei YUAN[2], Jun WANG[3], Yang CHEN[4], Panxi DAI[5], Adam H. SOBEL[6], Zhiyong MENG[1] & Ji NIE[1*]

[1] *Laboratory for Climate and Ocean-Atmosphere Studies, Department of Atmospheric and Oceanic Sciences, School of Physics, Peking University, Beijing 100871, China;*
[2] *Aviation Meteorological Center, Civil Aviation Administration of China, Beijing 100621, China;*
[3] *Key Laboratory of Regional Climate-Environment for Temperate East Asia (RCE-TEA), Institute of Atmospheric Physics, Chinese Academy of Sciences, Beijing 100029, China;*
[4] *State Key Laboratory of Severe Weather, Chinese Academy of Meteorological Sciences, Beijing 100081, China;*
[5] *Department of Atmospheric Science, School of Earth Sciences, Zhejiang University, Hangzhou 310027, China;*
[6] *Department of Applied Physics and Applied Mathematics and Lamont-Doherty Earth Observatory, Columbia University, New York, NY 10027, USA*

Abstract   In this study, we investigate the climate attribution of the 21·7 Henan extreme precipitation event. A conditional storyline attribution method is used, based on simulations of the event with a small-domain high-resolution cloud-resolving model. Large-scale vertical motion is determined by an interactive representation of large-scale dynamics based on the quasi-geostrophic omega equation, with dynamical forcing terms taken from observation-based reanalysis data. It is found that warming may lead to significant intensification of both regional-scale (10–14% K^{-1}, depending on convective organization) and station-scale precipitation extremes (7–9% K^{-1}). By comparing clustered convection organized by a localized surface temperature anomaly and squall-line convection organized by vertical wind shear, we further explored how convective organization may modify precipitation extremes and their responses to warming. It is found that shear convective organization is much more sensitive to large-scale dynamic forcing and results in much higher precipitation extremes at both regional and station scales than unorganized convection is. The clustered convection increases station-scale precipitation only slightly during heavy precipitation events. For regional-scale extreme precipitation sensitivity, shear-organized convection has a larger sensitivity by 2–3% K^{-1} than that of unorganized convection, over a wide temperature range, due to its stronger diabatic heating feedback. For the station-scale extreme precipitation sensitivity, no systemic dependence on convective organization is found in our simulations.

Keywords   Extreme precipitation, Global warming, Climate change attribution, Convective organization, Hourly precipitation

1.   Introduction

Around July 20, 2021, the Henan province of China was hit by an unprecedented rainfall event (named the 21·7 extreme precipitation event, Figure 1a). The peak hourly precipitation recorded by a weather station in Zhengzhou City reached 201.9 mm per hour (Figure 1b), setting a new record for Chinese mainland. The event claimed 398 deaths and missing persons, together with 120 billion Yuan of direct economic losses. The synoptic situation during the 21·7 event

---
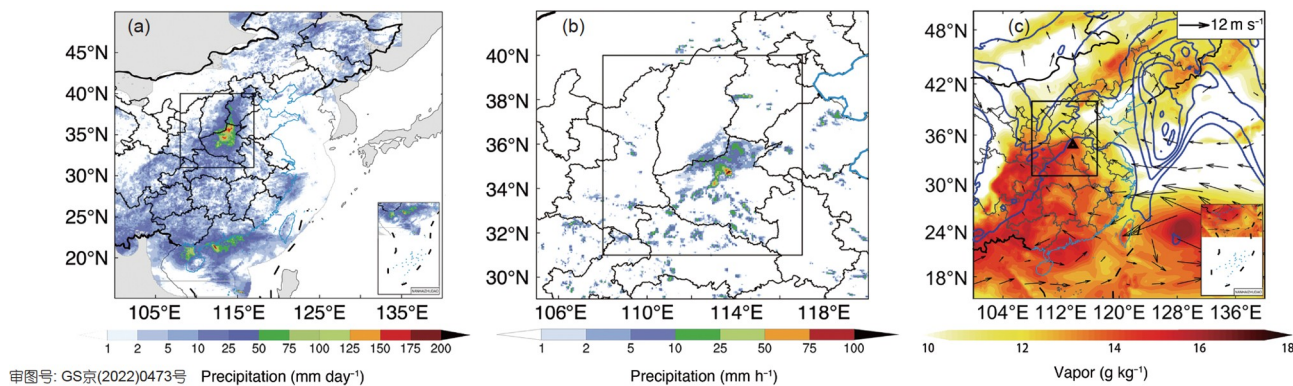
Figure 1 Observations of the 21·7 Henan extreme precipitation event. (a) 5-day mean precipitation (18 to 22 July) from CMA precipitation observations. (b) Hourly precipitation during LST 1600–1700 on 20 July. (c) The daily averaged 850 mb specific humidity (color shading), the 850 mb horizontal wind (black arrows), and the 150 mb potential vorticity (PV, blue contours, with an interval of 2 PVU) on 20 July. The black box indicates the region of interest with boundaries of 108°E–117°E and 31°N–40°N.

was apparently quite rare, and presumably a consequence of chaotic atmospheric dynamics. Considering that the global mean temperature has been raised by nearly 1 K by the last century, however, one may wonder how global warming might have affected the 21·7 extreme event in the present, or how further warming might affect events with the same synoptic-scale dynamics in the future.

The storyline approach to event attribution aims to discern the role of anthropogenic warming in extreme weather events in the presence of large uncertainties regarding the effects of warming on atmospheric circulation, but greater certainty about the thermodynamic effects (Trenberth et al., 2015; Shepherd, 2016; Lloyd and Oreskes, 2018; Lloyd and Shepherd, 2021). The storyline approach holds the large-scale circulation regime associated with a particular extreme event constant, and asks whether radiatively forced changes in the thermodynamic state, i.e., temperature and humidity, modify the event. Studies using this approach usually adopt event-based highly-conditional or "pseudo-global warming" simulations, in which the initial conditions are taken from the observed event, but large-scale temperature changes are applied (e.g., Lackmann, 2013). Though the storyline approach does not allow one to quantify changes in the probability of the event's occurrence, it is particularly useful in contexts where such quantification is problematic in any case due to uncertainties in dynamics (yet climate change impacts may still be large), and allows rich consideration of individual events, including dimensions beyond climate per se (Shepherd and Sobel, 2020).

A recently developed modeling method, the Column Quasi-Geostrophic (CQG) method (Nie and Sobel, 2016; Nie et al., 2016), has also been used for storyline event attribution (Nie et al., 2018, short as N18 hereafter). Designed to study the interactions between large-scale synoptic forcing and convective-scale processes, the CQG method has the advantage that it allows us to specify the large-scale synoptic

forcings while simulating the convection interactively, with the large-scale vertical motion influenced by both through the quasi-geostrophic omega equation. With this method, N18 quantified the amplification of extreme precipitation sensitivity due to diabatic heating feedbacks on large-scale ascent. The first goal of this study is to evaluate the potential intensification of the 21·7 event by climate warming, using the CQG method.

From the perspective of human hazards, regional-scale (i. e., several hundred kilometers) daily precipitation extremes and weather station-scale (i.e., several kilometers) hourly precipitation extremes are relevant to regional floods and flash floods, respectively. Physically speaking, regional and station precipitation extremes are often closely related, since an extreme rainfall event (such as the 21·7 event) may include both regional-scale and station-scale precipitation extremes. Most research studies treat them separately, however (e.g., IPCC AR5, AR6), and substantially different climate sensitivities have been found for the two types of extremes. For example, in many places station hourly precipitation extremes show similar hook-shape dependences on temperature (e.g., Lenderink and van Meijgaard, 2010; Fowler et al., 2021), while the climatic sensitivity of regional-scale daily precipitation has large geographic variability (e.g., Pfahl et al., 2017; Nie et al., 2020). While N18 mainly focus on regional-scale precipitation extremes, we examine both the regional and station precipitation extremes and their climate responses based on the 21·7 event.

Our second goal is to examine the influence of convective organization on the sensitivity of precipitation extremes to warming. In heavy rainfall events, convection is often organized into mesoscale systems (e.g., Houze, 2004; Zhai et al., 2007; Yin et al., 2022) by heterogeneities in boundary conditions, such as topography and surface types, or by environmental conditions such as wind shear. Organized convection differs significantly from unorganized convection in

its convective structures and precipitation characteristics (e. g., Tompkins, 2001; Singleton and Toumi, 2013; Muller, 2013). Moreover, the organization of convection may significantly change the interaction between convection and large-scale dynamics (e.g., Mapes, 2004; Mapes and Neale, 2011; Kuang, 2012). For example, Kuang (2012) showed that the extent of convective organization affects idealized "mock Walker cells" by altering the convective responses to large-scale temperature perturbations. Previous studies (Muller, 2013; Pendergrass et al., 2016) have compared the climate responses of extreme precipitation of unorganized and organized convection, but only under the idealization of radiative convective equilibrium (RCE). Here, we further examine how convective organization may impact both regional-scale and station-scale precipitation extreme responses to warming in a real extreme weather event, namely the 21·7 event, in which synoptic-scale forcing is strong and coupled to convective-scale dynamics, and the precipitation clearly showed organized patterns (Figure 1a and 1b).

2. Experimental design

We simulate the 21·7 event under a wide range of climates under the CQG modeling framework following similar approach to that of N18. Briefly speaking, we obtain the large-scale Quasi-Geostrophic (QG) synoptic forcing from reanalysis data and use it to drive a cloud-resolving model (CRM) representing precipitating region. The QG synoptic forcings are the adiabatic terms (advection of temperature and vorticity) in the QG omega (ω) equation (i.e., the first two right-hand-side terms of eq. (1) in N18), which are calculated from the ERA-5 reanalysis. The diabatic heating term (the third right-hand-side term of eq. (1) in N18) is not taken from observations, but rather simulated interactively by the CRM. The externally specified QG forcing and the diabatic heating obtained from the CRM are connected by the QGω equation, simplified by assuming a single horizontal wavenumber (Nie et al., 2016; N18). This coupling method allows the diabatic heating associated with the convection to feed back to the large-scale vertical motion and amplify the precipitation, while the synoptic-scale dynamics specified by the dry adiabatic terms remains constant.

The CRM used here is the System for Atmospheric Modeling version 6.8.2 (Khairoutdinov and Randall, 2003). The spatial domain is 128 km×128 km, with a 2-km horizontal resolution and doubly periodic horizontal boundaries. There are 64 vertical levels, with vertical grid spacings stretching from 50 m near the surface to about 500 m in the free troposphere. The lower boundary condition is an ocean surface. This idealization is acceptable since the surface fluxes are not important during the extreme event and the orographic lifting effect is included in the forcing (Nie et al.,

2016, 2018; Lu et al., 2021). To simulate the 21·7 event, we calculate the large-scale forcing (vorticity, temperature, and moisture horizontal advective terms) from reanalysis data (ERA-5, hourly and 0.25° resolution, Hersbach et al., 2020). After averaging over the region of interest (the black regional box covering the 21·7 event in Figure 1), they are used to force the CRM under the CQG framework. The orographic lifting is included as an imposed lower boundary condition of ω at 950 hPa obtained from the reanalysis, following a similar approach in Nie et al. (2016). The horizontal wavelength is set to be 2500 km, same as that in N18. To represent the impacts of climate, we change the background temperature and moisture by changing the prescribed surface temperature (T_s), with the large-scale forcing fixed. The control case (with T_s=301 K) is to reproduce the extreme precipitation in the 21·7 event under the current climate, and the perturbed cases, which have T_s varying from 297 to 307 K with an interval of 1 K, are used to simulate precipitation extremes with the same synoptic forcing under varying thermodynamic background states in a systematic way. In addition to the ERA-5 reanalysis, the Climate Prediction Center precipitation data (CPC, Chen et al., 2008) and the China Meteorological Administration precipitation data (CMA, a gauge-radar-satellite merged precipitation dataset on 5 km grids, Shen et al., 2018) are used for model validation.

This study consists of three groups of simulations to represent different sources of convective organization. The experiments of the first group (named HomoSST) have lower boundary conditions of uniform T_s, as in N18. Convection is unorganized in this group of experiments. The second group of experiments (named HeteSST, short for heterogeneous T_s distribution) is similar to the first one, except that T_s has a two-dimensional gaussian anomaly (with a half width of 21.3 km and an amplitude of 2 K). The anomaly is adjusted to have a domain average of zero, so that in each case the domain mean T_s is the same as that in the first group. The T_s anomaly mimics the heterogeneity in surface conditions in reality, such as might be caused by the urban heat island effect. Convection is organized into clusters over the high T_s regions (domain center) in this group of experiments. The third group of experiments (named Shear) is similar to the first one, except that a background boundary layer vertical wind shear is specified in the CRM domain. The wind shear is the same as the "Shear2" profile in Muller (2013), which is a decrease of u wind from 20 m s^{-1} at the surface to 0 m s^{-1} at 1 km height. It organizes convection into squall lines. In each group, a series of simulations is carried out with fixed QG forcing but varying T_s. For each case, the model is first to run for thirty days under RCE (i.e., without any forcing) for spin-up, then the QG forcing is applied simulating the period of 11th to 28th July. The experiments are summarized in Table 1. By comparing the simulations within

Table 1   The simulations in three experiment groups[a]

Group name	Setting	Convective organization	T_s
HomoSST	uniform T_s	random, unorganized convection	
HeteSST	T_s anomaly with a peak of 2 K	clustered convection over the high T_s region	297 K, ..., 301 K (control), ..., 307 K
Shear	vertical wind shear	squall-line convection	

a) The 301 K and 303 K cases, which are examined in details in section 4, have four ensemble runs with different initial random perturbations.

each group as functions of T_s, one may estimate the climatic sensitivity of extreme precipitation; and by comparing the simulations of the same T_s across the three groups, one may estimate the influence of convective organization on that sensitivity.

3.   Regional-scale precipitation extreme responses

The synoptic situation associated with the 21·7 extreme precipitation event is depicted in Figure 1 (detailed analyses in Su et al., 2021; Chyi et al., 2022; Bueh et al., 2022). The circulations associated with typhoon In-fa and the larger-scale monsoonal flow both transported a large amount of water vapor from the tropics to Henan province (Figure 1c). In the upper troposphere, a strong low-pressure trough, expressed as a positive potential vorticity (PV) anomaly, was located upstream of Henan province. The upper-level PV advection induced a large-scale QG forcing over Henan, leading to large-scale driven vertical ascent (Figure 2a). The orographic lifting by the Funiu Mountains also plays a critical role in determining the distribution and amounts of the heavy rainfall (Yin et al., 2022).

The CQG simulations are validated by comparing the simulation results with observations. Comparison of the precipitation series in three observational datasets and the control simulation (T_s=301 K case in the HomoSST group) shows that the control simulation well captures the 21·7 event (Figure 3). Furthermore, we compare the ω components in the reanalysis diagnosis and in the model simulations in Figure 2. The ω components in the reanalysis diagnosis are first computed using full QGω equation on the three-dimensional sphere grids before averaging over the regional box. In CQG, the component due to the QG forcing (ω_D) is calculated from the regionally averaged QG advective terms from a reanalysis using the single-wavenumber QGω equation, and the component due to diabatic heating (ω_Q) is calculated from the domain-mean diabatic heating from CRM. The components are also close to each other, further indicating that the simulations capture the main dynamics of the extreme events. The orographic lifting effect (ω_{bc}) is obvious; the simulated precipitation weakens by about one third if the orographic lifting (Figure 2g) is not included in the CQG forcings (Figure 3). Note that ω_Q is

significantly stronger than ω_D and ω_{bc}, indicating a large diabatic heating feedback. The corresponding diabatic heating feedback has a value of 3.1 (in the simulation, the value is 3.3 in reanalysis diagnosis), an outstanding number compared with the values of other extreme precipitation events in the same latitude (Figure 2d in Nie et al., 2020).

We first examine the responses of precipitation extremes to warming in the HomoSST group. The simulations may be interpreted as if the same synoptic situation as in the 21·7 event, represented by the state and evolution of the quasi-geostrophic potential vorticity field, were to occur under different climatic backgrounds. Here we only compare the 5-day (18 to 22 July) domain-mean precipitation (P) during the event, since the structure of the precipitation time series are similar among the simulations. As T_s increases from 297 K to 307 K, P increases exponentially (black line in Figure 4a). The sensitivity of P, calculated as the exponential growth rate locally at each T_s ($\frac{\delta \ln P}{\delta T_s}$, black line in Figure 4b), is similar to that in N18. As T_s increases, $\frac{\delta \ln P}{\delta T_s}$ increases from the Clausius-Clapeyron (CC) scaling ($\sim 7\%$ K^{-1}) to doubled CC scaling ($\sim 14\%$ K^{-1}), and then remains roughly constant as T_s further increases.

The precipitation may be approximated as the product of vertical ascent and column moisture (O'Gorman and Schneider, 2009):

$$P \approx -\frac{1}{g} \int \omega \frac{dq_s}{dp}\bigg|_{\theta^*} dp, \tag{1}$$

where $\frac{dq_s}{dp}\bigg|_{\theta^*}$ is the derivative of the saturation specific humidity (q_s) along a moist adiabat with the constant saturation equivalent potential temperature (θ^*) at each level, where the mass-weighted integration is taken over the troposphere (from the surface level to 100 hPa). Thus, one may decompose the sensitivity of precipitation extremes into thermodynamic and dynamic components (e.g., O'Gorman and Schneider, 2009; Dai and Nie, 2021; Yin et al., 2021). Given two simulations under different climates, the thermodynamic component is defined as $-\frac{1}{g} \int \omega \left(\delta \frac{dq_s}{dp}\bigg|_{\theta^*} \right) dp$, and the dynamic component is defined as $-\frac{1}{g} \int (\delta \omega) \frac{dq_s}{dp}\bigg|_{\theta^*} dp$, where δ
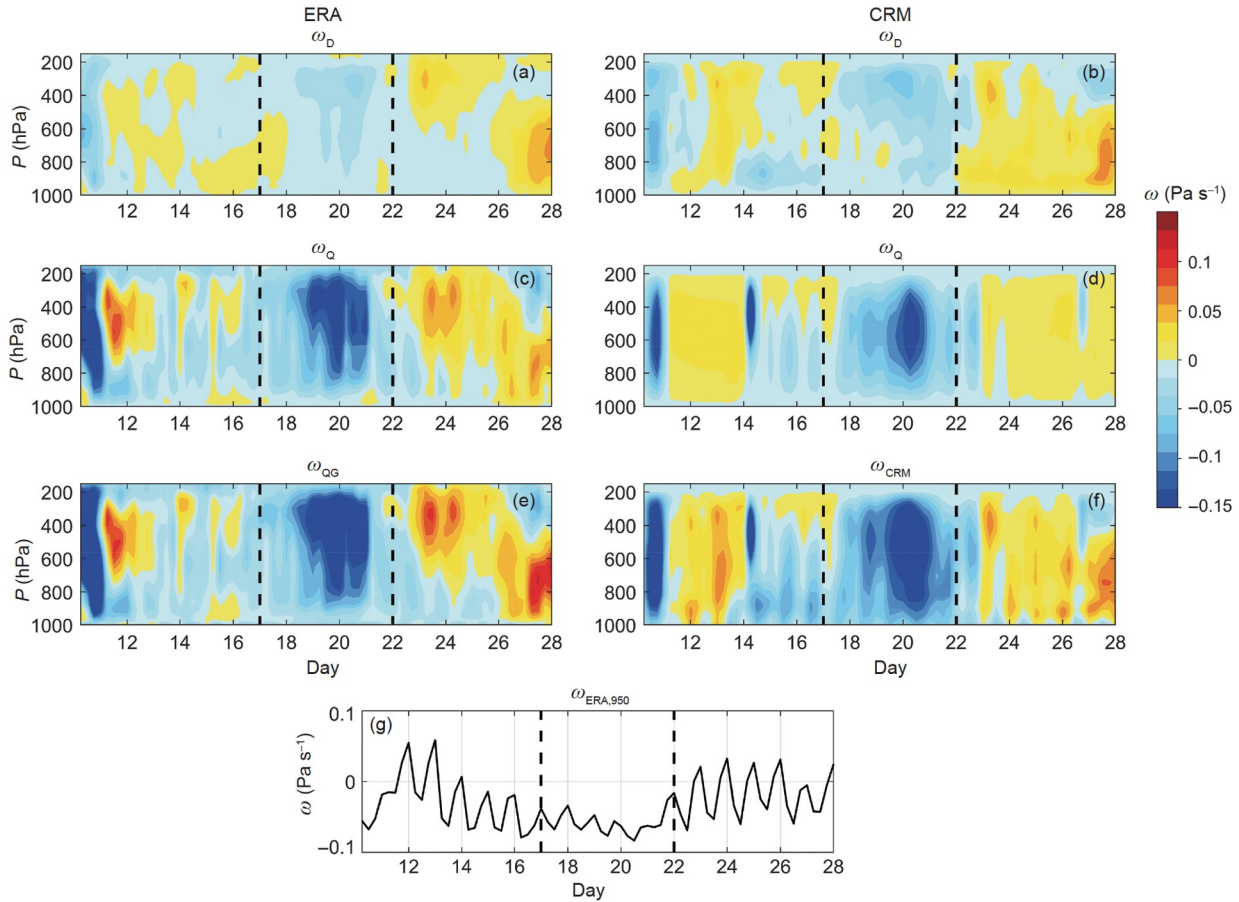
Figure 2 The omega components from the ERA-5 reanalysis (left column) and the CRM control simulation (the T_s=301 K case in the HomoSST group, right column). The first row is the component due to the dynamic QG forcing (ω_D), the second row is the component due to the diabatic heating (ω_Q), and the third component is the sum of the above two rows. (g) is the reanalysis ω at 950 hPa, which is used as boundary forcing in the CQG simulations.
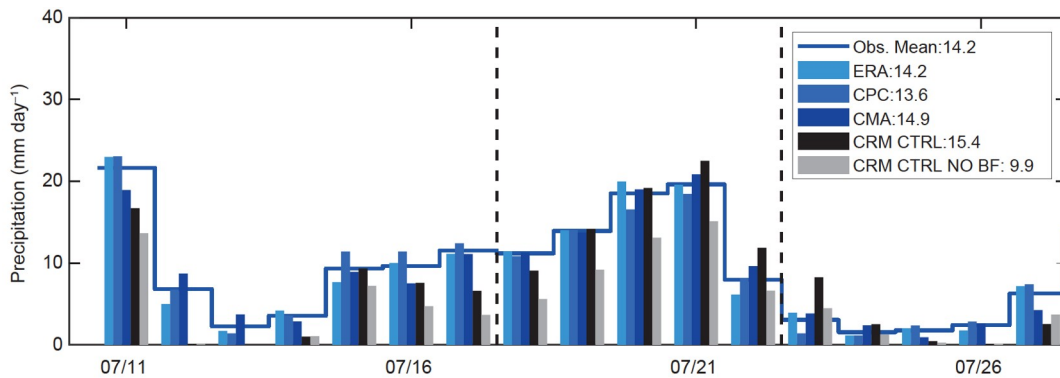

Figure 3 Time series of observed and simulated daily precipitation. The three blue bars denote the precipitation averaged over the regional box (black box in Figure 1) from the ERA-5 reanalysis, the CPC, and the CMA precipitation data, respectively. The blue line is the average of three observational data. The black bar denotes the control case in HomoSST group. The grey bar shows the results of the sensitivity experiment, which is same with the control case except the orographic lifting is not included in the simulation. The black dashed vertical lines indicate the 5-day period (18 to 22 July) of the event. The numbers in legend are the 5-day mean precipitation (with units of mm day^{-1}).

denotes the difference between the two climate states. The thermodynamic component, which represents the change in precipitation due to changes of column water vapor, is relatively constant over the T_s range here (black dashed line in Figure 4c). On the other hand, the dynamic component,

which represents the change of precipitation due to changes in vertical motion, increases with T_s (black solid line in Figure 4c), indicating stronger diabatic heating feedback at higher T_s.

Next, we examine the impacts of convective organization

Mean precipitation during event
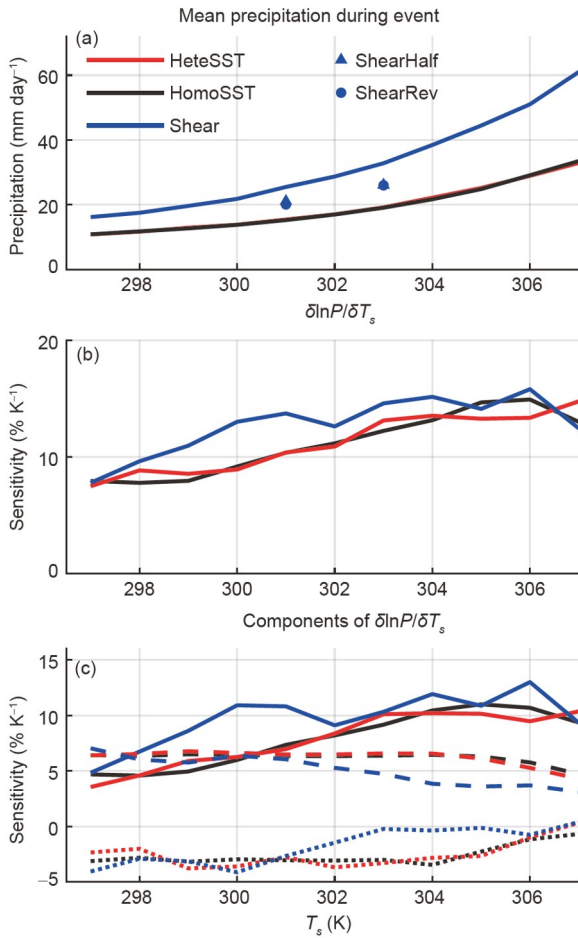
Figure 4 (a) Mean precipitation over the event (P) and (b) its climatic sensitivity $\left(\dfrac{\delta \ln P}{\delta T_s}\right)$ as functions of T_s. The blue triangles and filled circles in (a) denote the simulations of weak shear and reversed shear (ShearHalf and ShearRev, 301 K and 303 K runs). (c) shows the dynamic (solid lines) and thermodynamic (dashed lines) components of the sensitivity. The dotted lines in (c) indicate the residual term (which also may be interpreted as the precipitation efficiency term). In (a)–(c), the black, red, and blue colors denote the experiments in the HomoSST, HeteSST, and Shear groups, respectively.

Table 2 The domain-mean precipitation and precipitable water in the control simulations (T_s=301 K) under RCE and large-scale ascent

Variable	Scenario	HomoSST	HeteSST	Shear
Precipitation (mm day^{-1})	RCE	3.19	3.27	4.29
	large-scale ascent	20.69	21.26	34.40
Precipitable water (mm)	RCE	45.41	44.63	51.95
	large-scale ascent	46.51	46.99	62.09

teSST groups are close to each other both under RCE and large-scale ascent, while both values in the Shear group are significantly larger (Table 2). This indicates that convective organization by T_s heterogeneity has a small effect on the regional mean, while organization due to shear has a large effect. Interestingly, we observe that for the HeteSST cases, the clustering of convection in the center under large-scale ascent is not as obvious as that under RCE (Figure 5b, e and Figure 6b, 6e). Apparently, the role of T_s heterogeneity in convective organization is reduced by strong large-scale ascent. This point will be further confirmed in the following analyses.

How does convection respond to the QG forcing when it is organized, and does convective organization affect the sensitivity of precipitation extremes? Figure 4a summarizes the regional-mean precipitation over the event in all experiments in the three groups. The values in the HomoSST and HeteSST groups are very similar (Figure 4a), further suggesting that under strong large-scale ascent, T_s heterogeneity has a small effect on the total precipitation, perhaps because it is ineffective at organizing convection (Figure 5 and Figure 6). On the other hand, P in the Shear group is significantly greater than P in the other two groups, suggesting that squall-line convection is much more sensitive to the large-scale QG forcing and generates a larger diabatic heating feedback. The large diabatic heating feedback in the Shear group is consistent with its high precipitable water in the RCE state; as suggested by Nie et al. (2020) the diabatic heating feedback has a strong dependence on precipitable water. We carried out additional two simulations named ShearHalf and ShearRev to compare with the Shear group and test the effect of different wind shears. The wind shear in ShearHalf is similar to that in Shear, but half in magnitude (i.e., a decrease of u wind from 10 m s^{-1} at the surface to 0 m s^{-1} at 1 km height), and the resulting precipitation (blue triangles in Figure 4a) is in the middle of the HomoSST and Shear. The effect of background wind shear on domain averaged precipitation is cut in half when the shear is cut in half, further confirming the strong impacts of wind shear. The wind shear in ShearRev is reversed compared to that in Shear, with background u wind increasing from 0 m s^{-1} at the surface to 20 m s^{-1} at 1 km height. The resulting precipitation (blue circles in Figure 4a) is close to that of ShearHalf, indicating
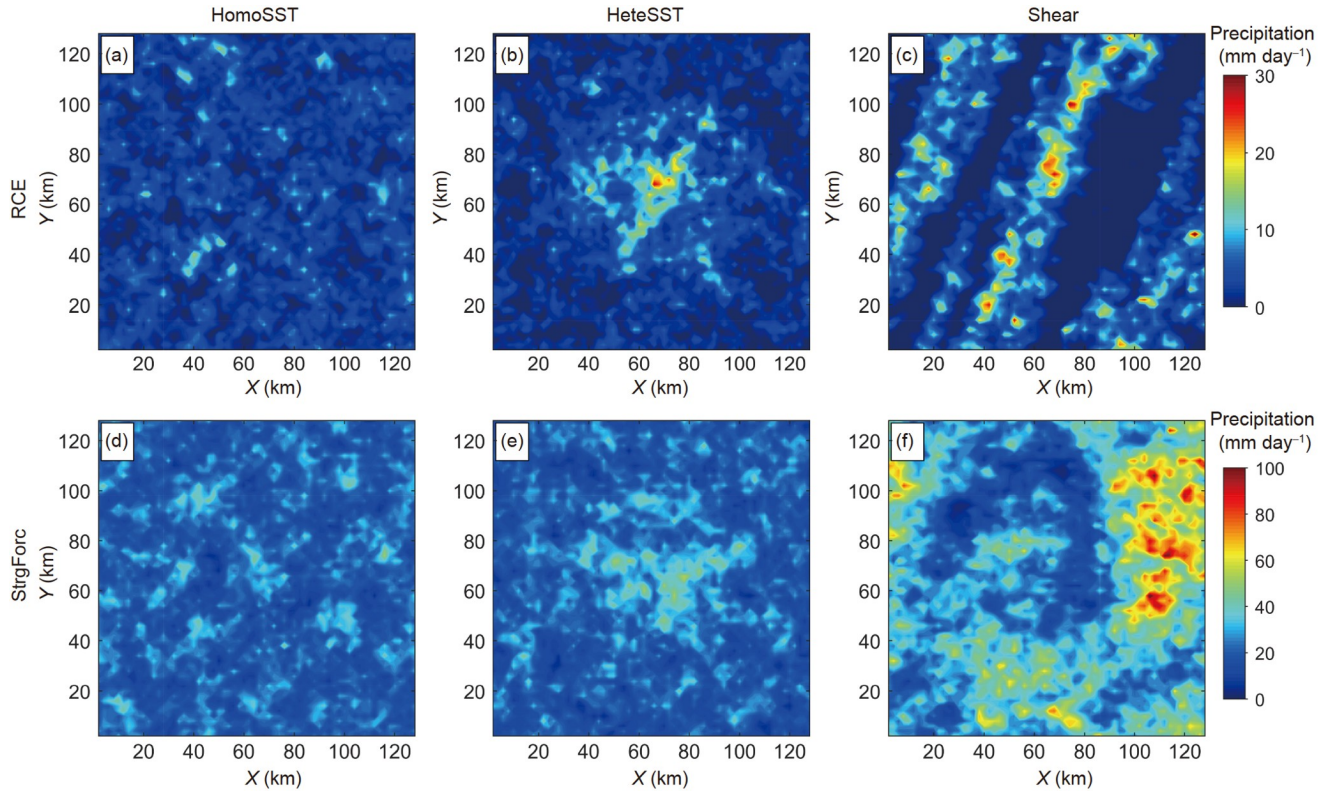
by comparing the results in the three experimental groups. Convection in the first group (HomoSST) is considered as not organized, while those in other two groups (HeteSST and Shear) are considered as organized according to their spatial distribution. As a reference, we first examine the spatial structure of the precipitation field in control T_s simulations under RCE (i.e., without large-scale ascent). Under RCE, precipitation is randomly distributed in HomoSST, clustered over the T_s anomaly in HeteSST, and organized into squall lines in Shear, as expected (Figure 5a–5c for precipitation, Figure 6a–6c for precipitable water). During the period of greatest precipitation during the event, the large-scale ascent leads to significant increases in both the domain-mean and grid-scale precipitation (Figure 5). The domain-mean precipitation and precipitable water in the HomoSST and He-

Figure 5   The ensemble (4 members) and time (2 days) average of precipitation for the control case in the HomoSST, HeteSST, and Shear group. The first row shows results under RCE, and the second row shows results during the period of greatest precipitation in the event (20 to 21 July). A movie for snapshots of convection can be found in the supporting material (https://link.springer.com).
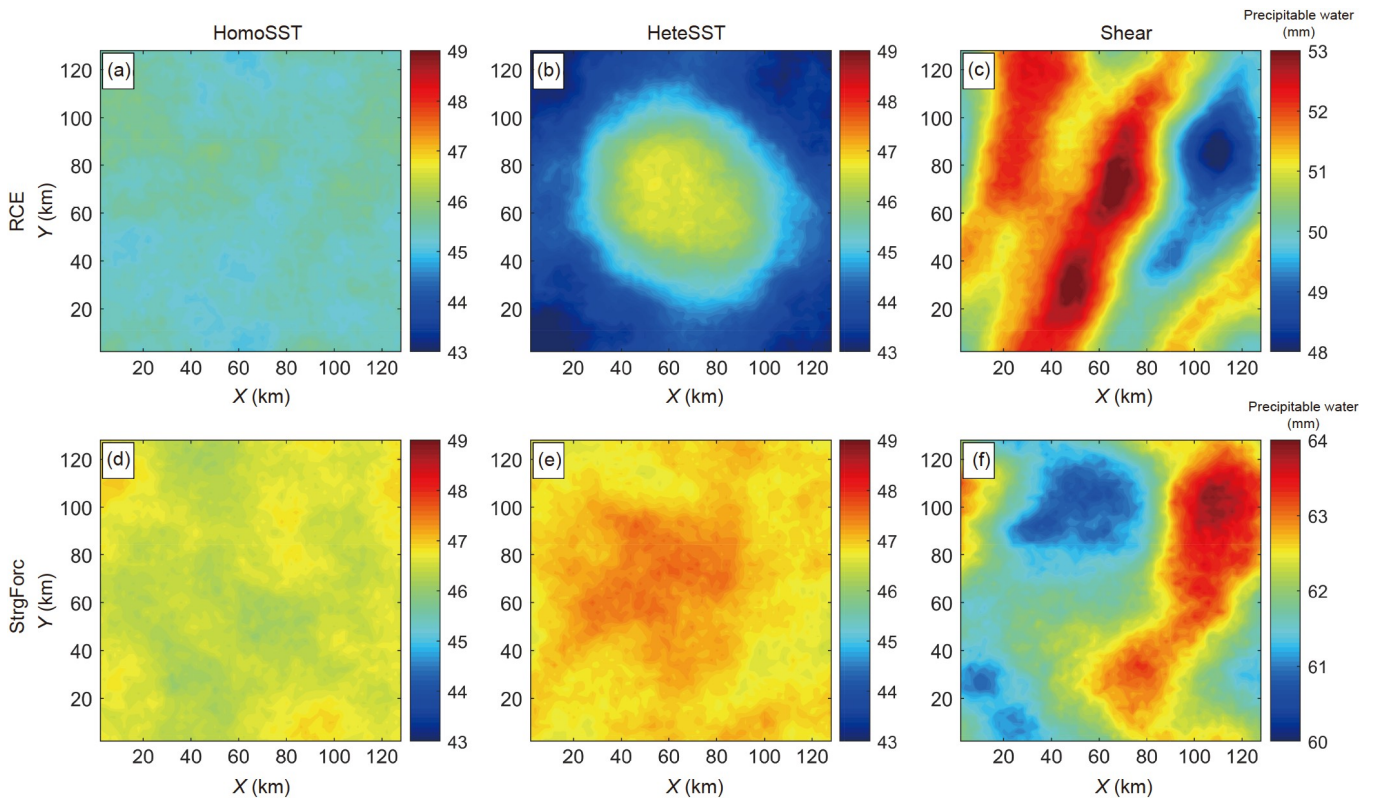
Figure 6   As in Figure 5, but for precipitable water. Note the color bars in (c) and (f) are different from the others for a better illustration.

that the amplification of precipitation by wind shear quantitatively depends on the profile of wind shear. For the sensitivity of precipitation (Figure 4b), $\frac{\delta \ln P}{\delta T_s}$ is similar for the HomoSST and HeteSST groups, while it is substantially larger for the Shear group over the T_s range of 298 K to 304 K. The decomposition of $\frac{\delta \ln P}{\delta T_s}$ (Figure 4c) shows that the thermodynamic components are similar among the three groups, while the dynamic components (equivalent with the diabatic heating feedback) account for their differences.

4. Grid-scale precipitation extreme responses

In this section, we examine the CRM grid-scale hourly precipitation extremes and their responses to warming with and without convective organization. We interpret these grid-scale values as analogous to station observations. Within each experiment group, we only compare the 301 K and 303 K cases, representing the current and a warmer climate respectively. To provide better statistics, each T_s setting has four ensemble runs with small random perturbations in their initial conditions.

We first examine the grid-scale hourly precipitation probability distribution functions (*pdf*s) in the current-climate simulations (Figure 7). Under RCE, the HeteSST *pdf* is only slightly greater than that of the HomoSST *pdf* over the high extreme end (dashed lines in Figure 7), consistent with the more intense convection over the positive T_s center (Figure 5b). The Shear *pdf* of extremes is significantly larger, indicating that squall-line convection organized by wind shear generates a much higher probability (one order of magnitude) of precipitation extremes of the magnitudes in this range. During the period of the event (18 to 22 July), the probability of precipitation extreme increases significantly in all the three groups (solid lines in Figure 7). The *pdf*s of HomoSST and HeteSST groups are very close to each other, again, confirming our previous observation that T_s heterogeneity has little effect in increasing precipitation extremes under strong large-scale ascent. On the contrary, wind shear can effectively organize convection and modify the grid-scale precipitation *pdf* regardless. The *pdf* computed from the CMA observations (black dotted line in Figure 7) is also plotted here for reference. However, note that the spatial resolution of CMA observation is 5 km, different from the 2 km CRM resolution.

Next, we examine the responses of grid-scale precipitation extremes during the 21·7 event to warming. Warming leads to significant increases of precipitation extremes for all three groups (Figure 8a). Two metrics are commonly used to quantify the increase of precipitation extremes to warming. The first metric measures the increase of precipitation in-
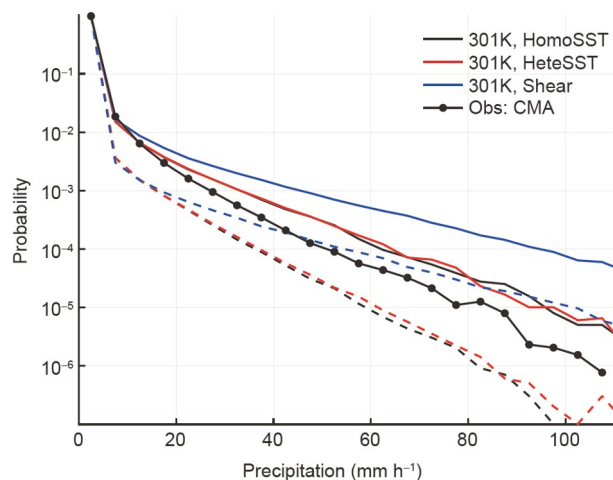

Figure 7 The probability distribution functions of grid-scale hourly precipitation of the control cases in the three experiment groups. The bin size of the *x* axis is 5 mm h^{-1}. Dashed lines denote results under equilibrium state of RCE runs and solid lines denote results under forcing during the extreme event (18 to 22 July). The black dot line is *pdf* from the CMA observation constructed over the regional box in Figure 1 during the 7·20 event (18 to 22 July).

tensity for a certain percentile (Figure 8b). The three groups show similar intensity increases, changing from ~9% K^{-1} at 99.9% percentile to ~7% K^{-1} at 99.999% percentile. The second metric measures the increase of probability for a certain precipitation intensity (Figure 8c). For example, for hourly precipitation of 100 mm h^{-1}, the 301 K and 303 K cases in the HomoSST group have probabilities of 1.9×10^{-5} and 5.6×10^{-5}, respectively. Thus, the increase in probability is $\frac{5.6 \times 10^{-5} - 1.9 \times 10^{-5}}{1.9 \times 10^{-5} \times 2K} \times 100\% = 97\%$ K^{-1}. The two metrics, although depicting the same change in the *pdf*, can lead to seemingly quite large differences of interpretation, and this sometimes may cause confusion (e.g., Titley et al., 2016). Caution should be used when comparing the results here to others in the literature.

5. Conclusions and discussion

Based on a storyline attribution method, involving idealized cloud-resolving simulations coupled to interactive large-scale dynamics via the quasi-geostrophic omega equation (the column quasi-geostrophic, or CQG method), we estimate the intensification of the 21·7 Henan extreme precipitation event due to global warming. Given a similar synoptic situation of the event, the warming and moistening of the atmospheric background state led to strengthened regional-scale (10–14% K^{-1}, depending on the convective organization) and station-scale precipitation extremes (7–9% K^{-1}). Furthermore, we investigate the impacts of convective organization on the extreme event and its climatic
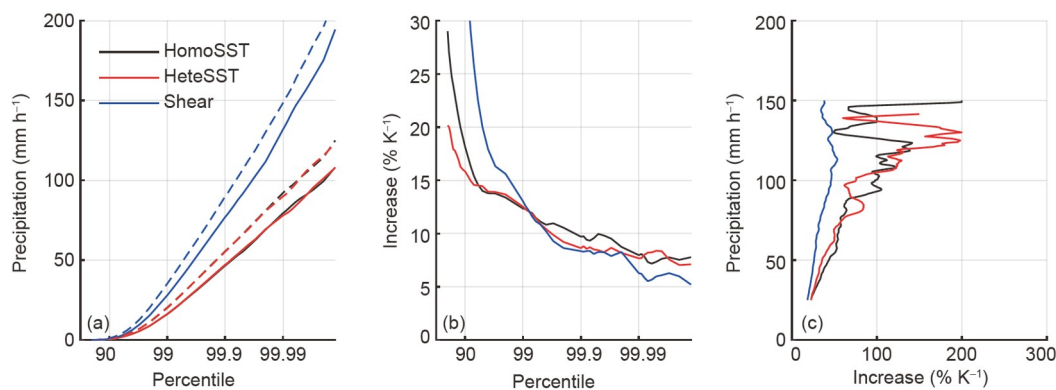
Figure 8   (a) Precipitation extremes for the 301 K cases (solid lines) and 303 K cases (dashed lines) in the three groups; (b) the fractional increases in precipitation for each percentile; (c) the fractional increases in probabilities for each precipitation intensity.

sensitivity by comparing the results of simulations with unorganized convection (HomoSST), clustered convection (HeteSST) driven by a surface temperature anomaly, and squall-line convection (Shear) driven by low-level wind shear. When considering regional-scale precipitation, the Shear convection is much more sensitive to large-scale forcing and results in much higher precipitation. The Shear convection also has a larger sensitivity to temperature due to its stronger diabatic heating feedback. When considering station precipitation, the Shear convection also has a much larger probabilities of extreme precipitation than the other two groups. Compared with unorganized convection, the HeteSST convection slightly increases station precipitation extremes over its high SST anomaly under RCE, but this effect diminishes during heavy precipitation driven by strong large-scale ascent. For the station-scale extreme precipitation sensitivity, there is no systematic dependence on convective organization in our simulations. The implication related with the 21·7 Henan extreme precipitation event is that the robust thermodynamic background changes due to warming over the past century has significant intensification on extreme precipitation like the 21·7 event, and the shear-induced convective organization in the 21·7 event plays critical role in generating the unprecedented regional and station precipitation extremes.

In extreme precipitation events, there are strong interactions crossing different scales, from large scale, to meso scale, and to convective scale. The results here clearly show the importance of meso-scale convective organization in linking the large-scale synoptic and convective scale dynamics. This study provides a quantitative assessment of how convective organization modifies the convective-scale precipitation probability distribution and the regional-scale convective sensitivity to large-scale synoptic perturbations. Our analysis shows that one important role of convective organization is that it increases the environmental moisture, both in regional means and in organized convective areas. The former affects the diabatic heating feedback, and the

latter protects local convective cells from dry air and generates more intense precipitation. The effects of convective organization may also depend on strength of large-scale ascent.

The CQG method is useful here in that it allows us to control the large-scale synoptic forcing and the type of convective organization separately. This separation cannot easily be achieved by traditional regional modeling methods, and makes the CQG method a potentially useful framework to explore cross-scale interactions in extreme events in future. For example, do our conclusions hold for convective organization caused by different wind shears or surface heterogeneities? In our simulations, we only considered the regional-mean effect of orographic lifting, which significantly contributes to the regional total rainfall of the event (Figure 3). The orography is also important in determining the precipitation distribution and organizing convection (e.g., Ding et al., 1978; Yin et al., 2022); these mesoscale effects shall be further explored. Compared with many previous studies that have examined the sensitivity of station-scale precipitation extremes under RCE (Muller, 2013; Ma et al., 2020), this study took a step forward in putting the station-scale precipitation extremes within a heavy rainfall event. More studies are needed, addressing other extreme events and convective organization conditions, to address the above questions.

References

Bueh C, Zhuge A R, Xie Z W, Gao Z T, Lin D W. 2022. Water vapor transportation features and key synoptic-scale systems of the "7.20" rainstorm in Henan Province in 2021 (in Chinese). Chin J Atmos Sci, 46: 725−744

Chen M Y, Shi W, Xie P P, Silva V B S, Kousky V E, Higgins R W,

Janowiak J E. 2008. Assessing objective techniques for gauge-based analyses of global daily precipitation. J Geophys Res, 113: D04110

Chyi D, He L F, Wang X M, Chen S. 2022. Fine observation characteristics and thermodynamic mechanisms of extreme heavy rainfall in Henan on 20 July 2021 (in Chinese). J Appl Meteorol Sci, 33: 1–15

Dai P X, Nie J. 2021. What controls the interannual variability of extreme precipitation? Geophys Res Lett, e2021GL095503

Ding Y H, Cai Z Y, Li J S. 1978. Study on the excessively heavy rainfall in Henan province early in August 1975 (in Chinese). Sci Atmos Sin, 2: 276–289

Fowler H J, Lenderink G, Prein A F, Westra S, Allan R P, Ban N, Barbero R, Berg P, Blenkinsop S, Do H X, Guerreiro S, Haerter J O, Kendon E J, Lewis E, Schaer C, Sharma A, Villarini G, Wasko C, Zhang X. 2021. Anthropogenic intensification of short-duration rainfall extremes. Nat Rev Earth Environ, 2: 107–122

Hersbach H, Bell B, Berrisford P, Hirahara S, Horányi A, Muñoz-Sabater J, Nicolas J, Peubey C, Radu R, Schepers D, Simmons A, Soci C, Abdalla S, Abellan X, Balsamo G, Bechtold P, Biavati G, Bidlot J, Bonavita M, Chiara G, Dahlgren P, Dee D, Diamantakis M, Dragani R, Flemming J, Forbes R, Fuentes M, Geer A, Haimberger L, Healy S, Hogan R J, Hólm E, Janisková M, Keeley S, Laloyaux P, Lopez P, Lupu C, Radnoti G, Rosnay P, Rozum I, Vamborg F, Villaume S, Thépaut J. 2020. The ERA5 global reanalysis. Q J R Meteorol Soc, 146: 1999–2049

Houze Jr R A. 2004. Mesoscale convective systems. Rev Geophys, 42: RG4003

Khairoutdinov M F, Randall D A. 2003. Cloud resolving modeling of the arm summer 1997 IOP: Model formulation, results, uncertainties, and sensitivities. J Atmos Sci, 60: 607–625

Kuang Z. 2012. Weakly forced Mock Walker cells. J Atmos Sci, 69: 2759–2786

Lackmann G M. 2013. The south-central US flood of May 2010: Present and future. J Clim, 26: 4688–4709

Lenderink G, van Meijgaard E. 2010. Linking increases in hourly precipitation extremes to atmospheric temperature and moisture changes. Environ Res Lett, 5: 025208

Lloyd E A, Oreskes N. 2018. Climate change attribution: When is it appropriate to accept new methods? Earths Future, 6: 311–325

Lloyd E A, Shepherd T G. 2021. Climate change attribution and legal contexts: Evidence and the role of storylines. Clim Change, 167: 1–3

Lu T, Cui X, Zou Q, Li H. 2021. Atmospheric water budget associated with a local heavy precipitation event near the central urban area of Beijing Metropolitan Region. Atmos Res, 260: 105600

Ma C, Yuan W, Ni J. 2020. Responses of mean and extreme precipitation to different climate forcing under Radiative-Convective Equilibrium. Adv Atmos Sci, 37: 377–386

Mapes B, Neale R. 2011. Parameterizing convective organization to escape the entrainment dilemma. J Adv Model Earth Syst, 3: M06004

Mapes B E. 2004. Sensitivities of cumulus-ensemble rainfall in a cloud-resolving model with parameterized large-scale dynamics. J Atmos Sci, 61: 2308–2317

Muller C. 2013. Impact of convective organization on the response of tropical precipitation extremes to warming. J Clim, 26: 5028–5043

Nie J, Dai P, Sobel A H. 2020. Dry and moist dynamics shape regional patterns of extreme precipitation sensitivity. Proc Natl Acad Sci USA, 117: 8757–8763

Nie J, Shaevitz D A, Sobel A H. 2016. Forcings and feedbacks on convection in the 2010 Pakistan flood: Modeling extreme precipitation with interactive large-scale ascent. J Adv Model Earth Syst, 8: 1055–1072

Nie J, Sobel A H. 2016. Modeling the interaction between quasigeostrophic vertical motion and convection in a single column. J Atmos Sci, 73: 1101–1117

Nie J, Sobel A H, Shaevitz D A, Wang S. 2018. Dynamic amplification of extreme precipitation sensitivity. Proc Natl Acad Sci USA, 115: 9467–9472

O'Gorman P A, Schneider T. 2009. The physical basis for increases in precipitation extremes in simulations of 21st-century climate change. Proc Natl Acad Sci USA, 106: 14773–14777

Pendergrass A G, Reed K A, Medeiros B. 2016. The link between extreme precipitation and convective organization in a warming climate: Global radiative-convective equilibrium simulations. Geophys Res Lett, 43: 11,445–11,452

Pfahl S, O'Gorman P A, Fischer E M. 2017. Understanding the regional pattern of projected future changes in extreme precipitation. Nat Clim Change, 7: 423–427

Shen Y, Hong Z, Pan Y, Yu J, Maguire L. 2018. China's 1 km merged gauge, radar and satellite experimental precipitation dataset. Remote Sens, 10: 264

Shepherd T G. 2016. A common framework for approaches to extreme event attribution. Curr Clim Change Rep, 2: 28–38

Shepherd T G, Sobel A H. 2020. Localness in climate change. Comp Studies South Asia Africa Middle East, 40: 7–16

Singleton A, Toumi R. 2013. Super-Clausius-Clapeyron scaling of rainfall in a model squall line. Q J R Meteorol Soc, 139: 334–339

Su A F, Lv X N, Cui L M, Li Z, Xi L, Li H. 2021. The basic observational analysis of "7.20" extreme rainstorm in Zhengzhou (in Chinese). Torr Rain Disast, 40: 445–454

Titley D W, Hegerl G, Jacobs K L, Mote P W, Paciorek C J, Shepherd J M, Shepherd T G, Sobel A H, Walsh J, Zwiers F W. 2016. Attribution of Extreme Weather Events in the Context of Climate Change. Washington D C: The National Academies Press

Tompkins A M. 2001. Organization of tropical convection in low vertical wind shears: The role of water vapor. J Atmos Sci, 58: 529–545

Trenberth K E, Fasullo J T, Shepherd T G. 2015. Attribution of climate extreme events. Nat Clim Change, 5: 725–730

Yin J, Gu H, Liang X, Yu M, Sun J, Xie Y, Li F, Wu C. 2022. A possible dynamic mechanism for rapid production of the extreme hourly rainfall in Zhengzhou City on 20 July 2021. J Meteorol Res, 36: 6–25

Yin Z H, Dai P X, Nie J. 2021. A two-plume convective model for precipitation extremes. Adv Atmos Sci, 38: 957–965

Zhai G Q, Zhou L L, Wang Z. 2007. Analysis of a group of weak small-scale vortexes in the planetary boundary layer in the mei-yu front. Adv Atmos Sci, 24: 399–408

(Responsible editor: Guixing CHEN)